Article

An optical lattice with sound

https://doi.org/10.1038/s41586-021-03945-x

Received: 27 April 2021

Accepted: 23 August 2021

Published online: 10 November 2021

Check for updates

Yudan Guo[1,2], Ronen M. Kroeze[1,2], Brendan P. Marsh[2,3], Sarang Gopalakrishnan[4], Jonathan Keeling[5] & Benjamin L. Lev[1,2,3]✉

Quantized sound waves—phonons—govern the elastic response of crystalline materials, and also play an integral part in determining their thermodynamic properties and electrical response (for example, by binding electrons into superconducting Cooper pairs)[1–3]. The physics of lattice phonons and elasticity is absent in simulators of quantum solids constructed of neutral atoms in periodic light potentials: unlike real solids, traditional optical lattices are silent because they are infinitely stiff[4]. Optical-lattice realizations of crystals therefore lack some of the central dynamical degrees of freedom that determine the low-temperature properties of real materials. Here, we create an optical lattice with phonon modes using a Bose–Einstein condensate (BEC) coupled to a confocal optical resonator. Playing the role of an active quantum gas microscope, the multimode cavity QED system both images the phonons and induces the crystallization that supports phonons via short-range, photon-mediated atom–atom interactions. Dynamical susceptibility measurements reveal the phonon dispersion relation, showing that these collective excitations exhibit a sound speed dependent on the BEC–photon coupling strength. Our results pave the way for exploring the rich physics of elasticity in quantum solids, ranging from quantum melting transitions[5] to exotic 'fractonic' topological defects[6] in the quantum regime.

Ultracold neutral atoms confined in optical lattices have been a fruitful platform for 'emulating' the itinerant motion of electrons in crystals[7]. Optical lattices, however, lack a crucial feature of real crystal lattices, which is elasticity. Real crystal lattices vibrate, deform in response to electrons, and transmit stresses; in contrast, optical lattices are non-dynamical. Elasticity has recently seen a revival of interest, motivated by developments such as 'fracton-elasticity duality'[6]. While the motion of ions in real crystals is classical, a natural question is how elasticity would change in the presence of strong quantum zero-point motion of the atoms in the crystal; few controlled experimental studies of this regime exist. We realize a system that combines crystalline elasticity with quantum-degenerate motion, in the form of a compliant optical lattice arising from the crystallization of Bose-condensed Rb atoms. While mimicking the effect of phonons in static optical lattices has been proposed[8], our method yields a continuum of phonon modes akin to those in solid-state materials.

Crystallization is the spontaneous breaking of the continuous translational symmetry of space. Due to this symmetry-breaking, a crystal has a manifold of physically distinct equilibrium states, which are related to one another by global translations (that is, by sliding the entire crystal). Global, zero-momentum ($k = 0$) translations connect these equilibrium states and cost no free energy. Additionally, crystals with local interactions have a continuum of finite-k modes with arbitrarily low energies: these modes, called phonons, involve locally sliding the crystal by an amount that varies slowly in space with a period $2\pi/k$. Because global translations cost no energy, while local translations do, a crystal is rigid, and responds globally to local stresses. The phonon excitation branch, which is the Goldstone mode of the broken translational symmetry, governs the elastic properties of crystals. The properties of the phonon branch are intimately tied to those of topological defects, such as dislocations, which have recently been identified as fractonic excitations. In contrast, for symmetry-breaking arising from all-to-all interactions (or other sufficiently long-range interactions), while the $k = 0$ zero mode may remain in place, there is a gap to all $k \neq 0$ excitations. This gives topological defects an extensive energy cost, and thus, in these long-range crystals, any nontrivial elastic response is frozen out. (When the atoms forming a crystal are already Bose-condensed, so that the crystal is a 'supersolid', there are additional superfluid Goldstone modes. These superfluid modes are associated with the $U(1)$ phase of the condensate itself and also exist in the absence of a lattice[9,10]. Sound propagation and diffusion have been studied with strongly interacting fermions[11,12].)

The primarily contact interactions among Rb atoms do not support crystallization. Optical cavity photons, however, can mediate interactions that do support crystallization, as follows. We begin by considering a pump field that is oriented transverse to a Fabry–Pérot cavity axis that is far detuned from all but a single resonance. Above a critical threshold pump strength, a density wave (DW) polariton condensate[13] forms via a superradiant (Hepp–Lieb–Dicke) phase transition: the N intracavity atoms cooperatively scatter pump photons into the cavity, forming a coherent optical state, while concomitantly the atoms adopt one of two chequerboard configurations of the $\lambda/2$-period lattice[14,15]. This $\cos k_r x \cos k_r z$ lattice is formed by the interference of the pump field with the emergent cavity field. The two-photon scattering process excites the $k = 0$ BEC into a superposition of $|k_x, k_z\rangle = |\pm k_r, \ \pm k_r\rangle$

[1]Department of Physics, Stanford University, Stanford, CA, USA. [2]E. L. Ginzton Laboratory, Stanford University, Stanford, CA, USA. [3]Department of Applied Physics, Stanford University, Stanford, CA, USA. [4]Department of Physics, The Pennsylvania State University, University Park, PA, USA. [5]SUPA, School of Physics and Astronomy, University of St Andrews, St Andrews, UK. ✉e-mail: benlev@stanford.edu

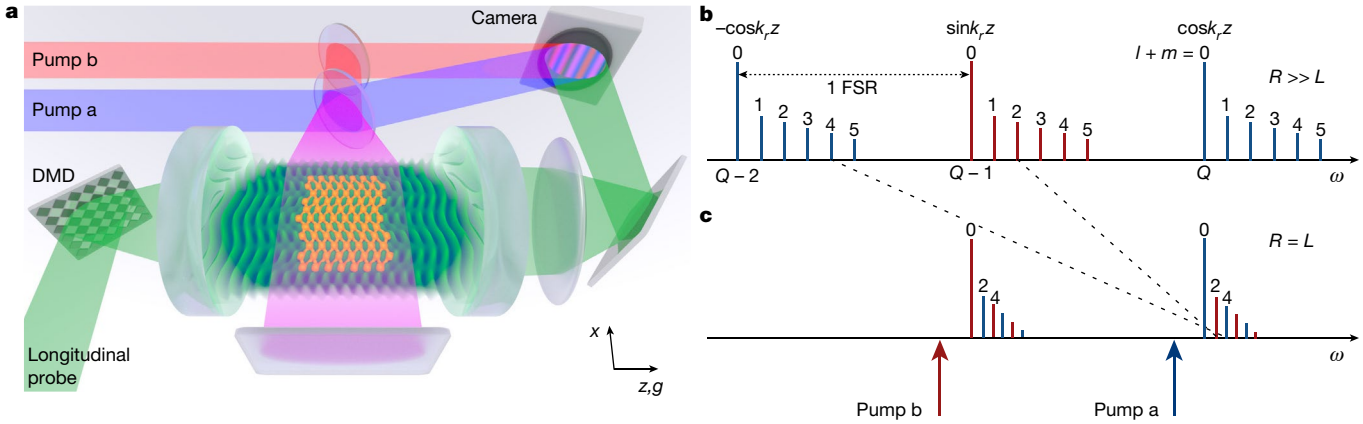

Fig. 1 | Transverse, double-pumped confocal cavity quantum electrodynamics system coupled to a BEC. a, Sketch of the vibrating atomic density wave (orange) created inside the confocal cavity field (green). Blue and red transverse pump fields are combined (purple) and retroreflected to form a standing wave. A beamsplitter directs some pump light onto a charge coupled device (CCD) camera to serve as a local oscillator (LO) for the holographic imaging of the spatially dependent phase and amplitude of the cavity emission. A digital micromirror device (DMD) injects patterns of light for measuring dispersion relations: this light longitudinally pumps the cavity along $\hat{z}$ at frequency ω and transverse wavevector $k_\perp$ along $\hat{x}$. The momentum distribution of the atoms is measured in time-of-flight via absorption imaging along $\hat{x}$ (not shown). **b**, Spectrum of a cavity whose radius of curvature R is much greater than its length L, which thus operates in the resolved-mode regime of single or few-mode cavities. Families of modes with fixed longitudinal mode number Q have the same longitudinal phase offset; they differ in phase by $\pm\pi/2$ from families with $Q\pm1$ one FSR away. **c**, The confocal cavity mode spectrum showing even parity families. (Frequency-degenerate transverse modes, labelled by the sum of their indices $l+m$, are dispersed in ω for ease of viewing.) The modes in each family alternate in longitudinal phase. The blue and red arrows indicate the transverse pumps a and b, respectively.

momentum modes, where $\hat{x}$ ($\hat{z}$) is the pump (cavity) axis, the pump and cavity fields are of wavelength $\lambda \approx 780$ nm, and $k_r = 2\pi/\lambda \approx 8$ rad μm^{-1} is the recoil momentum; $\hbar\omega_r = \hbar^2 k_r^2/2m \approx 2\pi\hbar \times 3.8$ kHz is the recoil energy, where $2\pi\hbar$ is Planck's constant. The state is stable if the pump frequency ω_P is red-detuned by $\Delta_C = \omega_P - \omega_C < 0$ from the cavity resonance ω_C.

Such single-mode experiments have enabled the exploration of a variety of quantum collective phenomena[16–19], but do not have a continuous translational symmetry and are thus neither rigid nor elastic. A continuous translational symmetry can be restored if one adds a second cavity mode. For example, one emerges from the phase difference of forward- and backward-travelling waves in a ring-cavity geometry[20–23], or from the amplitude ratio when crossing two cavities[24,25]. In both these cases, this gives rise to a continuous $U(1)$ family of steady states, which can be related by continuous global displacement of the atoms. We will explain this mechanism below. However, since in these experiments the interactions are mediated by only a few cavity modes, the interactions are infinite-range, so the 'crystal' does not allow for non-trivial elastic deformations.

Coupling atoms to far more than two modes is necessary to create a compliant lattice that may, for example, lead to superfluids with quantum liquid crystalline structure or exhibiting Meissner-like effects and Peierls instabilities[20,21,26,27]. One can superpose many degenerate modes to form compact supermodes—localized photon wavepackets[18,28]. Exchanging these localized photons leads to finite-range interactions and momentum exchange[28–30]. As such, when a multimode cavity is combined with a double-pumping scheme to engineer a $U(1)$ symmetry, a fully fledged Goldstone mode with a dispersion relation should emerge. If using a BEC, the result would be a supersolid with phonons. (Phonons have also been proposed and sought via the refractive index change of atoms coupled to strong light fields[31–33] and exist as natural modes in ion traps[34].)

In what follows, we first review how a $U(1)$ symmetry can be engineered by double-pumping in the context of a two-mode cavity[30]; we then extend it to multimode cavities. We consider two pump fields, labelled 'a' and 'b', each detuned by Δ_C from one of two cavity modes spaced one free spectral range (FSR) apart. Figure 1a sketches a transversely double-pumped cavity, while Fig. 1b shows the spectrum of a cavity whose length L greatly exceeds its mirrors' radius of curvature R. Each pump induces an interaction between atom pairs. The combined interaction takes the form:

$$U^{\mathrm{sm}}_{\mathrm{total}} \propto U^{\mathrm{sm}}_{\mathrm{a}} \cos k_r z \cos k_r z' + U^{\mathrm{sm}}_{\mathrm{b}} \sin k_r z \sin k_r z', \tag{1}$$

where $U_i^{\mathrm{sm}}(x,x') = \eta_i^2 \cos k_r x \cos k_r x'/\Delta_C$ is the interaction strength induced by each pump field of intensity $\propto\Omega_i^2$ and is negative under red detuning. The two-photon coupling is $\eta_i \equiv g_0\Omega_i/4\,\Delta^i_A$, and for notational simplicity, we will drop the (x,x') arguments of U_i^{sm}. The coupling strength of a single atom to the cavity field is g_0, and the pumps are detuned from the atomic level by Δ^i_A, which are much greater than Δ_C and the transition linewidth. The change from cosine to sine reflects the shift by $\lambda/2$ in the longitudinal field profile as the modes' longitudinal index Q changes by one; Q is the number of optical half-wavelengths separating the mirrors. The interaction strengths become equal when $\eta_a = \eta_b \equiv \eta$, with the result that $U^{\mathrm{sm}}_a = U^{\mathrm{sm}}_b \equiv U^{\mathrm{sm}}$ and the interaction has a continuous translational symmetry along $\hat{z}$: $U^{\mathrm{sm}}_{\mathrm{total}} = U^{\mathrm{sm}} \cos[k_r(z-z')]$.

To create a lattice where phonons exist, we extend this double-pumping scheme to a multimode cavity of confocal configuration $L = R = 1$ cm. Figure 1c shows the confocal mode spectrum, which contains families of degenerate modes of either all-even or all-odd parity[35]. We pump two even mode families spaced one FSR apart. As in the single-mode case, the longitudinal mode profile alternates between cosine and sine. In addition, higher-order transverse modes in the same family also alternate in longitudinal profile. The interaction driven by the pumps is therefore $U^{\mathrm{mm}}_{\mathrm{total}} \propto U^{\mathrm{mm}}_{\mathrm{a}} + U^{\mathrm{mm}}_{\mathrm{b}}$, where

$$U^{\mathrm{mm}}_{\mathrm{a}} = U_0 \cos k_r z \cos k_r z' + U_2 \sin k_r z \sin k_r z' \tag{2}$$

$$U^{\mathrm{mm}}_{\mathrm{b}} = U_0 \sin k_r z \sin k_r z' + U_2 \cos k_r z \cos k_r z'. \tag{3}$$

As discussed in the Supplementary Information, the interaction strengths $U_{0,2}$ are[28–30]

$$U_{0,2}/U^{\mathrm{sm}} \approx \frac{\mathrm{e}^{-\Delta r/\xi}}{\sqrt{\Delta r/\xi}} \pm \cos\left[\frac{\mathbf{r}\cdot\mathbf{r}'}{w_0^2/2}\right]. \tag{4}$$

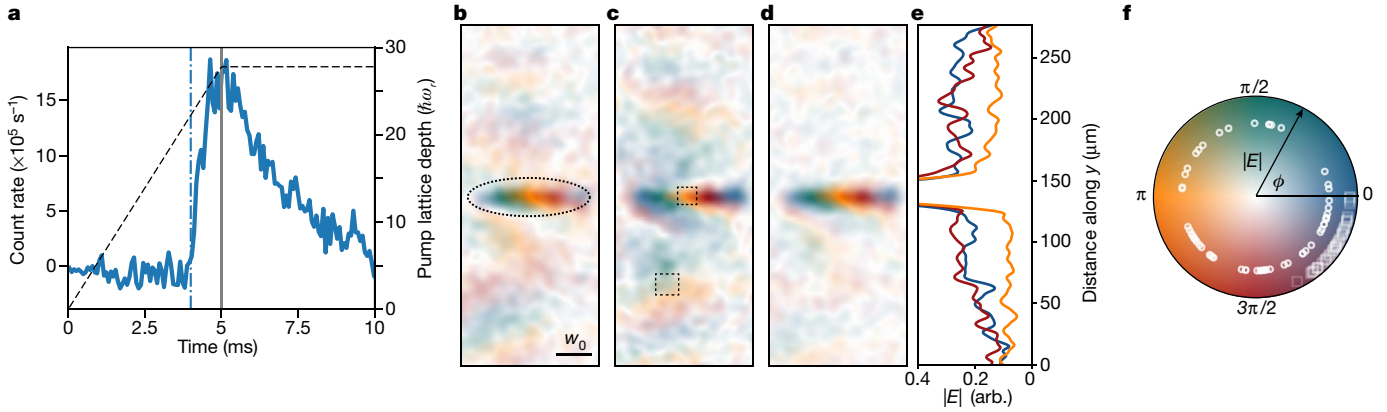

Fig. 2 | Efficacy of double-pumping scheme. a, Cavity emission intensity versus time (left axis); background counts have been subtracted. The pump lattice depth $\propto \eta^2$ (right axis, dashed black line) is linearly ramped through the superradiant threshold ($\eta^2 = \eta_{\mathrm{th}}^2$ at the blue vertical dash-dotted line) before being held constant at the measurement time (grey vertical solid line). **b**–**e**, Evidence that the non-local interaction is cancelled by double-pumping. Holograms of emission from a double-pumped confocal cavity with either the blue pump LO (**b**) or the red pump LO (**c**) illuminating the camera. The BEC image appears as the bright rainbow-like stripe. Its position in panel **b** is indicated by the dotted oval. While this emission arises from the local interaction—the first term in equation (4)—emission outside this region is due to photons mediating the non-local interaction (the second term). Note that the linear phase gradient (rainbow-like feature) in the local emission is an artefact caused by nonlinearities arising at strong pumping strengths: While large strengths of $\eta^2/\eta_{\mathrm{th}}^2 \approx 10$ are needed to obtain high signal-to-noise in these images, far weaker strengths $\eta^2/\eta_{\mathrm{th}}^2 \leq 1.25$, at which these nonlinearities are negligible, are sufficient for taking the dispersion data in Figs. 3 and 4. See Supplementary Information for details. **d**, The absence of the non-local interaction is revealed by taking the digital sum of these holograms. **e**, This is more clearly shown by integrating each of these images along $\hat{x}$ and comparing the intensity level of non-local emission in the single-pumped traces (blue for panel **b**, red for **c**) to the double-pumped trace (orange). The emission from the non-local interaction is much reduced due to the cancellation of the non-local parts in $U_{\mathrm{a}}^{\mathrm{mm}}$ and $U_{\mathrm{b}}^{\mathrm{mm}}$ when both pumps are present. **f**, A scatter plot of the shot-to-shot phase of the DW polariton under the single (square) and double (circle) pumping scheme is overlaid on the colour scale for the field amplitude $|E|$ and phase ϕ. This phase is the difference between the local and non-local phase in the emission regions indicated by, for example, the dashed boxes in panel **c**. (Symbols in each set are offset in radius for clarity; 60 points are shown for each.) The near-random distribution about 2π for the double-pumping scheme, as opposed to the clumping of the single-pumped phases, illustrates the emergence of the $U(1)$ symmetry. This demonstrates that in panels **d**, **e** the non-local interaction is sufficiently cancelled; see Supplementary Information for derivation.

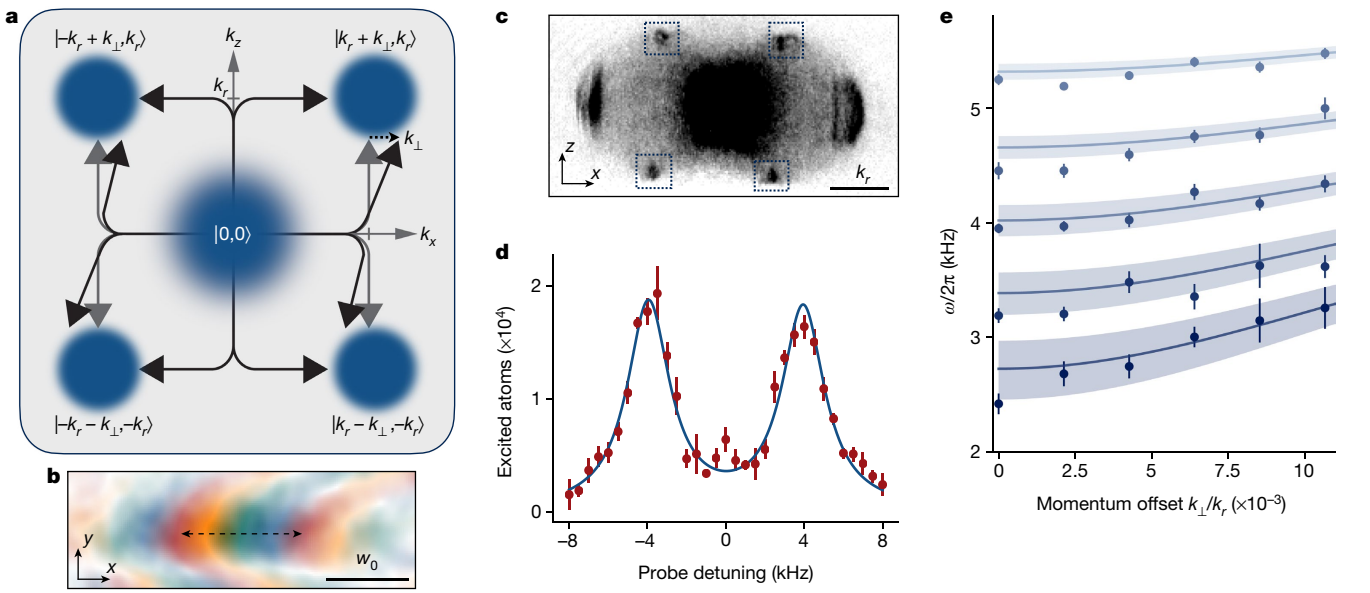

Fig. 3 | Soft-mode dispersion of density-wave polaritons below threshold. a, The two-photon scattering process excites atoms by receiving one momentum kick from a pump photon along $\pm\hat{x}$ and another from a cavity photon along $\pm\hat{z}$. The transverse momentum of the higher-order cavity modes shifts the $\pm\hat{x}$ momentum by an amount $\pm k_\perp$. Shown is one possible momentum state. **b**, While transversely pumping below threshold, we stimulate a soft mode with a particular $k_\perp$ by seeding the cavity longitudinally. An example of a seed field is shown here, as imaged by the transmission from an empty cavity. Cavity and imaging distortions curve the $k_\perp x$ phase fronts. **c**, Below-threshold absorption image of atoms in time-of-flight after a small fraction have been Bragg-stimulated into the four peaks indicated by squares. The other two peaks arise from the pump lattice alone. **d**, Example Bragg scattering spectrum showing the number of scattered atoms versus probe detuning from ω_{P}. Data are the sum of atoms within the squares in panel **c** for $\eta^2/\eta_{\mathrm{th}}^2 = 0.5$ and $k_\perp/k_r \approx 2.5 \times 10^{-3}$. A double Lorentzian (blue curve) is fit to the data, and the excitation energy is half the separation between peaks. Vertical bars represent standard error here and below. **e**, Dispersion relation ω versus $k_\perp$ for momenta offset from zero by k_r. The curves are plotted for pump strengths ranging from $\eta^2/\eta_{\mathrm{th}}^2 = 0.3$ at the top (lightest blue) to 0.7 at bottom (darkest blue) in steps of 0.1. Each column of data at fixed $k_\perp$ shows a softening roton mode as the supermode DW polariton condenses at threshold. Data are compared to parameter-free theory curves (with error bands) derived from the theory developed in the Supplementary Information.

The waist of the lowest-order cavity mode is $w_0 = 35\,\mu m$. The first term is the local interaction with $\Delta r = |\mathbf{r} - \mathbf{r}'|$ and a range $\xi \gtrsim 2\,\mu m$; $\xi \approx 5\,\mu m$ for the data presented and is set by the number of degenerate modes supported by the confocal cavity and Δ_C (ref. [28]). The second term is the non-local interaction. It cancels in the double-pump scheme, yielding both the desired local interaction and the $U(1)$ translational symmetry:

$$U^{mm}_{total} = U^{sm}\frac{e^{-\Delta r/\xi}}{\sqrt{\Delta r/\xi}}\cos k_r \Delta z. \quad (5)$$

A local mirror image term, omitted above, does not play a role in this work because we place the atoms in only one half-plane of the cavity.

We demonstrate the cancellation of the non-local contribution to the cavity-mediated interaction by imaging the phase and amplitude of the above-threshold superradiant emission under double-pumping; see Methods regarding holographic imaging. Figure 2b, c show the cavity emission from photons mediating U^{mm}_a and U^{mm}_b, respectively. The local interaction created by the atoms gives rise to the image of the BEC in the emergent lattice. That is, the interaction manifests as an emitted image because it is the local light in the cavity that mediates the interaction and this same light leaks out of the cavity[28]; see also Supplementary Information. The emission surrounding the BEC is from the non-local interaction[29,30]. This non-local interaction is cancelled under double pumping. This manifests as an image without non-local emission $\propto U^{mm}_{total}$, which we can obtain through the digital summation of the single-local-oscillator (LO) images. Indeed, this is what we observe in Fig. 2d and in the line integrations of Fig. 2e. The resulting emergence of the $U(1)$ symmetry manifests as a random distribution of DW phases each time the system is pumped above threshold. This is shown in Fig. 2f; see Methods for measurement procedure and discussion. A representative time trace of cavity emission is shown in Fig. 2a.

As a first study of this translationally symmetric system, we focus on the below-threshold spectroscopy of the k-dependent, normal (roton) dispersion where there is no lattice and thus no phonon. We will then show how the excitation spectrum changes above threshold in the presence of the emergent lattice. In single-mode cavities, a roton instability at $k = k_r$ results in a DW polariton condensate at threshold[36]. In a confocal cavity, by contrast, momentum-exchange mediated by the local interaction allows atoms to scatter into a range of states with $|k_\perp|$ added to $|k_r|$ along $\pm\hat{x}$, as illustrated in Fig. 3a. Consequently, the supermode DW polariton shows broad roton minima softening near k_r. We can probe the dispersion around this point by stimulating the cavity at a particular $k_\perp \geq 0$. This is done by injecting a longitudinal pump field whose amplitude and phase has been programmed by the digital micromirror device (DMD) to be $\propto e^{ik_\perp x}$ (ref. [37]); see Fig. 1a for an illustration. Figure 3b shows an example field pattern. We can stimulate values close to the characteristic momentum scale of this multimode cavity $\zeta \equiv \xi^{-1} \approx 0.02 k_r$.

We measure the dispersion of these k-dependent roton soft modes by cavity-enhanced Bragg stimulation. While pumping below threshold, we stimulate the cavity with the longitudinal probe field at a particular $k_\perp$ set by the DMD. Atoms are more efficiently scattered into the Bragg peaks of Fig. 3a when the frequency and wavevector of the probe field match the roton dispersion, which varies with pump strength $\propto \eta$. We directly absorption-image these scattered atoms in time-of-flight, as shown in Fig. 3c. Summing the atoms in all four peaks, we can plot the excitation spectrum for a given $k_\perp$ and η; see Fig. 3d. Figure 3e compiles the excitation frequencies. As η increases, we see the rotons soften and become more strongly dispersive—that is, display a stronger k dependence. At $\eta \to 0$, the dispersion is that of atomic DWs set by the atomic mass; with increasing η, atomic DWs mix with photons to form DW-polaritons, leading to a steeper dispersion; see Supplementary Information.

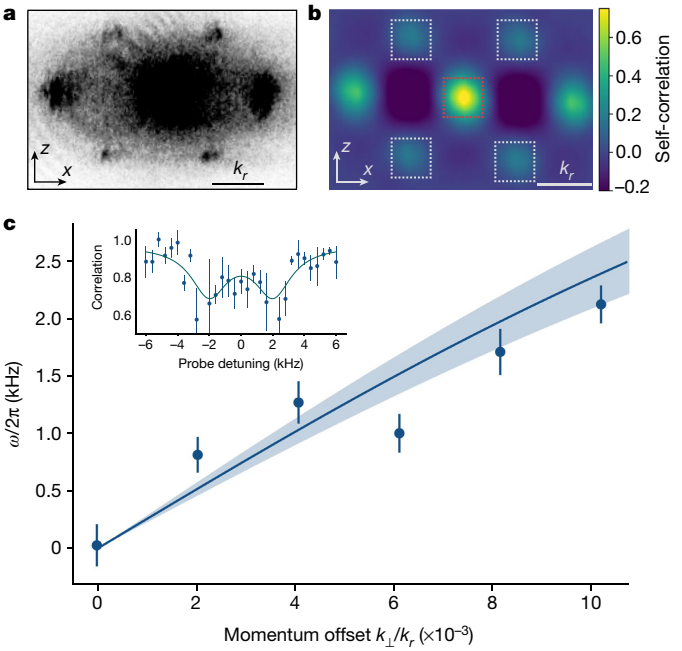

Fig. 4 | Goldstone dispersion relation $\omega(k_\perp)$. a, Example above-threshold time-of-flight image that records the momentum distribution $\rho(\mathbf{k})$. **b**, The self-correlation analysis yielding $\langle\rho(\mathbf{k}+\delta\mathbf{k})\rho(\mathbf{k})\rangle$. The white dashed squares indicate regions of interest for extracting the correlation strength associated with the chequerboard lattice. The correlation strength is calculated by normalizing the sum of the values in white squares by that in the central red dashed square. **c**, The dispersion relation curve (blue) is overlaid using the theory presented in the Supplementary Information and is parameter-free. The data are plotted with momenta offset from zero by k_r. They are consistent with a linear dispersion for $k_\perp \ll \zeta$. The pump strength is $\eta^2/\eta^2_{th} = 1.25$. The error band (light blue) represents one-sigma error in the theory parameters. Inset shows an example dynamic susceptibility spectrum obtained from self-correlation analyses taken for $k_\perp/k_r \approx 0.01$. Correlations decrease on resonance because the momentum structure factor differs from the $|0, 0\rangle$ state due to the addition of $k_\perp$.

We now demonstrate that the dispersion of the lattice phonon branch is gapless and linear. We do so by measuring the Goldstone dispersion of the phonon modes of the lattice that forms above threshold. We again use cavity-enhanced Bragg stimulation to measure dynamic susceptibility $\omega(k_\perp)$. Above threshold, however, the Bragg peaks of the DW polariton condensate are too populous to discern the additional Bragg-scattered atoms. Moreover, $k_\perp \ll k_r$ and our maximal time-of-flight is too short to discern the additional $\pm k_\perp$ from the spread in k about the peaks. We instead employ a self-correlation analysis of the momentum distribution to extract the phonon mode resonances; see Methods. For example, Fig. 4b is the self-correlation of the momentum image in Fig. 4a for a particular ω and $k_\perp$. The result is the Goldstone mode dispersion curve in Fig. 4c. As derived in the Supplementary Information, the low-k dispersion is linear: $\omega(k_\perp) = v_s|k_\perp|$, with a sound speed $v_s \simeq \sqrt{\hbar\omega_r[1 + (\eta/\eta_{th})^2](1/2m + E_1/\zeta^2)}$, where the cavity-mediated interaction strength is $E_1 = -8\eta^2 N/\Delta_C$. One may note that typically $E_1/\zeta^2 \gg 1/2m$, so the phonon dispersion is predominantly set by the cavity-mediated interactions. These phonon excitations have a sound velocity of 16 cm s^{-1}, $10^4\times$ slower than that in, for example, copper at room temperature. The theory curve contains no free parameters.

The self-consistent cavity optical lattice and atomic DW create a compliant lattice, while individual atoms remain itinerant within the lattice. In real space, the acoustic phonon modes manifest as a sliding motion of the lattice along the cavity axis $\hat{z}$, modulated along the $\hat{x}$ direction with wavevector $k_\perp$, corresponding to a transverse phonon mode; this motion is illustrated in the Supplementary Video. (Here,

we use 'transverse' to refer to the relative directions of displacement versus wavevector, rather than with respect to the cavity axes.)

Note that instead of imaging the momentum distribution, we could also have imaged the phonon through the pattern of light emitted from the cavity (see Supplementary Information for an example). In this sense our system acts as an unusual 'active' quantum gas microscope, in which the cavity fields mediate interactions that support phonons, while their emission provides spatial information about the atomic density profile.

Adding other atomic spin states or species within this dynamic lattice would more directly mimic electrons in traditional solid-state systems. Replacing the BEC with a degenerate Fermi gas might provide opportunities to study the electron–phonon physics related to polarons[38] in a context complementary to previous studies[39–41] or to study metallic transport in strange metals beyond the semiclassical approximation of long-lived quasiparticles[42]. Moreover, the dual role of itinerant coherent atoms forming a compliant dynamical lattice may also provide access to regimes not attainable in solid-state systems, for example, to resolve phonon number states to perform quantum acousto-optical experiments with supersolids.

Online content

Any methods, additional references, Nature Research reporting summaries, source data, extended data, supplementary information, acknowledgements, peer review information; details of author contributions and competing interests; and statements of data and code availability are available at https://doi.org/10.1038/s41586-021-03945-x.

1. Kittel, C. *Introduction to Solid State Physics* (Wiley, 2004).
2. Chaikin, P. M. & Lubensky, T. C. *Principles of Condensed Matter Physics* (Cambridge Unive. Press, 1995).
3. Tinkham, M. *Introduction to Superconductivity* (Dover, 2004).
4. Grimm, R., Weidemüller, M. & Ovchinnikov, Y. B. in *Advances In Atomic, Molecular, and Optical Physics* Vol. 42 (eds. Bederson, B. & Walther, H.) 95–170 (Elsevier, 2000).
5. Beekman, A. J. et al. Dual gauge field theory of quantum liquid crystals in two dimensions. *Phys. Rep.* **683**, 1–110 (2017).
6. Pretko, M. & Radzihovsky, L. Fracton-elasticity duality. *Phys. Rev. Lett.* **120**, 195301 (2018).
7. Bloch, I., Dalibard, J. & Zwerger, W. Many-body physics with ultracold gases. *Rev. Mod. Phys.* **80**, 885–964 (2008).
8. González-Cuadra, D., Grzybowski, P. R., Dauphin, A. & Lewenstein, M. Strongly correlated bosons on a dynamical lattice. *Phys. Rev. Lett.* **121**, 090402 (2018).
9. Stamper-Kurn, D. M. et al. Excitation of phonons in a Bose-Einstein condensate by light scattering. *Phys. Rev. Lett.* **83**, 2876–2879 (1999).
10. Pethick, C. & Smith, H. *Bose-Einstein Condensation in Dilute Gases* (Cambridge Univ. Press, 2002).
11. Patel, P. B. et al. Universal sound diffusion in a strongly interacting Fermi gas. *Science* **370**, 1222–1226 (2020).
12. Brown, P. T. et al. Bad metallic transport in a cold atom Fermi-Hubbard system. *Science* **363**, 379–382 (2018).
13. Carusotto,, I. & Ciuti, C. Quantum fluids of light. *Rev. Mod. Phys.* **85**, 299–366 (2013).
14. Kirton, P., Roses, M. M., Keeling, J. & Dalla Torre, E. G. Introduction to the Dicke model: from equilibrium to nonequilibrium, and vice versa. *Adv. Quantum Technol.* **2**, 1800043 (2018).
15. Mivehvar, F., Piazza, F., Donner, T. & Ritsch, H. Cavity QED with quantum gases: new paradigms in many-body physics. Preprint at https://arxiv.org/abs/2102.04473 (2021).
16. Klinder, J., Keßler, H., Bakhtiari, M. R., Thorwart, M. & Hemmerich, A. Observation of a superradiant Mott insulator in the Dicke-Hubbard model. *Phys. Rev. Lett.* **115**, 230403 (2015).
17. Landig, R. et al. Quantum phases from competing short- and long-range interactions in an optical lattice. *Nature* **532**, 476–479 (2016).
18. Kollár, A. J. et al. Supermode-density-wave-polariton condensation with a Bose–Einstein condensate in a multimode cavity. *Nat. Commun.* **8**, 14386 (2017).
19. Kroeze, R. M., Guo, Y. & Lev, B. L. Dynamical spin-orbit coupling of a quantum gas. *Phys. Rev. Lett.* **123**, 160404 (2019).
20. Gopalakrishnan, S., Lev, B. L. & Goldbart, P. M. Emergent crystallinity and frustration with Bose Einstein condensates in multimode cavities. *Nat. Phys.* **5**, 845–850 (2009).
21. Gopalakrishnan, S., Lev, B. L. & Goldbart, P. M. Atom-light crystallization of Bose–Einstein condensates in multimode cavities: Nonequilibrium classical and quantum phase transitions, emergent lattices, supersolidity, and frustration. *Phys. Rev. A* **82**, 043612 (2010).
22. Mivehvar, F., Ostermann, S., Piazza, F. & Ritsch, H. Driven-dissipative supersolid in a ring cavity. *Phys. Rev. Lett.* **120**, 123601 (2018).
23. Schuster, S., Wolf, P., Ostermann, S., Slama, S. & Zimmermann, C. Supersolid properties of a Bose-Einstein condensate in a ring resonator. *Phys. Rev. Lett.* **124**, 143602 (2020).
24. Léonard, J., Morales, A., Zupancic, P., Esslinger, T. & Donner, T. Supersolid formation in a quantum gas breaking a continuous translational symmetry. *Nature* **543**, 87–90 (2017).
25. Léonard, J., Morales, A., Zupancic, P., Donner, T. & Esslinger, T. Monitoring and manipulating Higgs and Goldstone modes in a supersolid quantum gas. *Science* **358**, 1415–1418 (2017).
26. Ballantine, K. E., Lev, B. L. & Keeling, J. Meissner-like effect for a synthetic gauge field in multimode cavity QED. *Phys. Rev. Lett.* **118**, 045302 (2017).
27. Rylands, C., Guo, Y., Lev, B. L., Keeling, J. & Galitski, V. Photon-mediated Peierls transition of a 1D gas in a multimode optical cavity. *Phys. Rev. Lett.* **125**, 010404 (2020).
28. Vaidya, V. D. et al. Tunable-range, photon-mediated atomic interactions in multimode cavity QED. *Phys. Rev. X* **8**, 011002 (2018).
29. Guo, Y., Kroeze, R. M., Vaidya, V. D., Keeling, J. & Lev, B. L. Sign-changing photon-mediated atom interactions in multimode cavity quantum electrodynamics. *Phys. Rev. Lett.* **122**, 193601 (2019).
30. Guo, Y. et al. Emergent and broken symmetries of atomic self-organization arising from Gouy phase shifts in multimode cavity QED. *Phys. Rev. A* **99**, 053818 (2019).
31. Lewenstein, M. et al. in *AIP Conference Proceedings* Vol. 869 (eds Roos, C., Häffner, H. & Blatt, R.) 201–211 (AIP, 2006).
32. Ostermann, S., Piazza, F. & Ritsch, H. Spontaneous crystallization of light and ultracold atoms. *Phys. Rev. X* **6**, 021026 (2016).
33. Dimitrova, I. et al. Observation of two-beam collective scattering phenomena in a Bose-Einstein condensate. *Phys. Rev. A* **96**, 051603 (2017).
34. Monroe, C. et al. Programmable quantum simulations of spin systems with trapped ions. *Rev. Mod. Phys.* **93**, 025001 (2021).
35. Siegman, A. E. *Lasers* (University Science Books, 1986).
36. Mottl, R. et al. Roton-type mode softening in a quantum gas with cavity-mediated long-range interactions. *Science* **336**, 1570–1573 (2012).
37. Papageorge, A. T., Kollár, A. J. & Lev, B. L. Coupling to modes of a near-confocal optical resonator using a digital light modulator. *Opt. Express* **24**, 11447–11457 (2016).
38. Devreese, J. T. & Alexandrov, A. S. Fröhlich polaron and bipolaron: recent developments. *Rep. Prog. Phys.* **72**, 066501 (2009).
39. Hu, M.-G. et al. Bose polarons in the strongly interacting regime. *Phys. Rev. Lett.* **117**, 055301 (2016).
40. Jørgensen, N. B. et al. Observation of attractive and repulsive polarons in a Bose-Einstein condensate. *Phys. Rev. Lett.* **117**, 055302 (2016).
41. Yan, Z. Z., Ni, Y., Robens, C. & Zwierlein, M. W. Bose polarons near quantum criticality. *Science* **368**, 190–194 (2020).
42. Werman, Y., Kivelson, S. A. & Berg, E. Nonquasiparticle transport and resistivity saturation: a view from the large-N limit. *npj Quant. Mater.* **2**, 7 (2017).
43. Kollár, A. J., Papageorge, A. T., Baumann, K., Armen, M. A. & Lev, B. L. An adjustable-length cavity and Bose-Einstein condensate apparatus for multimode cavity QED. *New J. Phys.* **17**, 043012 (2015).

Methods

BEC preparation

BEC production proceeds as in ref. [43]. To shape the BEC for this experiment, we use the same dynamical trap shaping technique as employed in our previous work[30]. A nearly pure BEC is created in state $|F=1,\ m_F=-1\rangle$. A harmonic potential consisting of two crossed beams of wavelength 1,064 nm forms a trap of frequencies $(\omega_x, \omega_y, \omega_z) = 2\pi \times [52.6(2), 52.8(2), 91.5(4)]$Hz. The BEC population is $N = 4.1(3) \times 10^5$ and has Thomas–Fermi radii of $(R_x, R_y, R_z) = [12.3(2), 12.2(2), 7.1(1)]$ μm. Finally, by changing the dither pattern of the trapping beams perpendicular to the pump, the trap shape is adiabatically deformed to produce an elongated gas of 93 μm along the pump direction $\hat{x}$. A harmonic potential in the other two directions is maintained with similar trap frequencies in the other two directions. The centre-of-mass of its density distribution lies at $\mathbf{r}_{cm}$ = (49 μm, 35 μm) along $\hat{x}$ and $\hat{y}$ with respect to the cavity centre.

Cavity, pump lasers and frequency locks

The confocal cavity is vibrationally stabilized using the method presented in ref. [43]. It is 1 cm long and has a radius of curvature $R = 1$ cm, resulting in a waist of its $TEM_{0,0}$ mode of $w_0 = 35$ μm. Its finesse is 5.5×10^4, yielding a cavity linewidth of $\kappa = 2\pi \times 137$ kHz. With a single-atom, single-mode coupling g_0 of $2\pi \times 1.47$ MHz, the single-atom, single-mode cooperativity is $C = 2g_0^2/\kappa\gamma = 5$, where the atomic linewidth is $\gamma = 2\pi \times 6$ MHz. Assuming a supermode enhancement factor of ~10 (proportional to the inverse local interaction length scale ξ)[28], the supermode single-atom cooperativity is $C^* \approx 50$.

The 780-nm pump beams are each derived from a frequency-doubled 1,560-nm fibre amplifier and seed laser; see Supplementary Information for a schematic. The relative frequency between the two 1,560-nm seed lasers is stabilized with respect to a frequency source oscillating at half of the cavity free spectral range ~7.5 GHz. This frequency difference is controlled using a proportional-integral loop filter with feedback applied to seed 'b'. A portion of the doubled 780-nm light from seed 'a' is used as the illumination beam for the DMD. The DMD reflects this light into the path of the longitudinal cavity injection beam. Acousto-optical modulators are used to stabilize the intensity and adjust the relative detuning between the beams. Additional 1,560-nm light from seed 'a' is used to stabilize the science cavity using the Pound–Drever–Hall technique. The two pumps are detuned from the $5\ ^2S_{1/2}|2,-2\rangle$ to $5\ ^2P_{3/2}$ transition by 96 GHz and 111 GHz, respectively. Throughout the experiments, the pumps are equally detuned from the relevant cavity resonances by $\Delta_C^a = \Delta_C^a \equiv \Delta_C = -2\pi \times 50$ MHz.

Lattice calibration and pump balancing

We calibrate the lattice depth of pump beams by performing Kapitza–Dirac diffraction of the BEC. The phase of the pump fields at the BEC is controlled by the retroreflection mirror shared by the pump beams. Measuring the lattice depth of the combined pump beams, we adjust the translation stage on which this mirror is mounted to match the phases of the pump lattices at the position of the atoms. We note that the beat length of the two pump lattices (separated in optical frequency by 15 GHz) is ~5 mm, much larger than the atomic cloud size. Therefore, small mechanical fluctuations from the mirror mount will not cause the lattice to become out-of-phase at the atoms. The difference in recoil energy from this difference in frequency is on the order of ~0.1 Hz and thus negligible, as is the change in wavelength.

To bring into balance the cavity-mediated interactions induced by each pump, we perform a sequence of single-pump self-organization experiments. We linearly ramp up each beam in 5 ms and note the time at which the superradiant threshold is reached. The interaction strength can then be balanced by adjusting the ramp rate such that superradiance on a single FSR occurs at the same time for each beam. This ensures that the Raman coupling rate from each FSR is balanced, that is, $\eta_a = \eta_b$, which then balances the cavity interaction strength for each pump.

Holographic reconstruction of cavity emission

To perform the holographic imaging (spatial heterodyne detection) of the cavity emission, we follow the procedure established in refs. [29,44] for a single pump field and extend it to the case of two pumps. Above threshold, the cavity emission has optical frequency content at both ω_a and ω_b (the two pump frequencies), separated by one FSR. To fully reconstruct the cavity electric field, therefore, one must illuminate the camera with two large LO beams at frequencies ω_a and ω_b at different angles with respect to the propagation direction of the cavity emission. This is illustrated in Fig. 1a in the main text. The interference between LO and the cavity emission produces an image with an intensity $I_h(\mathbf{r})$ that may be expressed as

$$I_h(\mathbf{r}) = \sum_{i=a,b} |E_{c,i}(\mathbf{r})|^2 + |E_{LO,i}(\mathbf{r})|^2 + 2\chi_i |E_{c,i}(\mathbf{r}) E_{LO,i}(\mathbf{r})| \cos[\Delta\mathbf{k}_i \cdot \mathbf{r} + \Delta\phi_i(\mathbf{r}) + \delta_i],$$

where we have ignored the fast oscillating term at $\omega_b - \omega_a$, and $E_{c,i}$ and $E_{LO,i}$ are the cavity fields and LO fields for the two FSRs, respectively. Reduction of fringe contrast is characterized by the factor χ_i. The additional phase terms δ_i account for the overall phase drift between the LO beams and the cavity emission in each experimental realisation due to technical fluctuations of the apparatus. Because of the angle difference, information from the cavity fields $E_{c,a}$ and $E_{c,b}$ are encoded in spatial wavevectors $\Delta\mathbf{k}_a$ and $\Delta\mathbf{k}_b$, respectively. Assuming the cavity field varies slowly over the spatial scale $2\pi/|\Delta\mathbf{k}_i|$, we may then extract the cavity field amplitudes $|E_{c,i}(\mathbf{r})|$ and phase profiles $\Delta\phi_i(\mathbf{r}) + \delta_i$ by demodulating the image at $\Delta\mathbf{k}_i$.

By using this scheme—an LO at each frequency but at different spatial wavevectors—we take a single spatial heterodyne image that simultaneously allows us to reconstruct the intracavity field for each resonance. The phase of the non-local emission should differ by π in the two images and indeed this signal cancels in their digital sum, as shown in Figs. 2d, e in the main text.

Generation of longitudinal probe with the DMD

The DMD plane is set at approximately the Fourier plane of the cavity centre by using a 100-mm focal length in-vacuum plano-convex lens. The phase aberration of the DMD and misalignment of the illumination beam must be calibrated out of the field images sent into the cavity. We first calibrate these aberrations with an out-of-vacuum setup, similar to that used in ref. [37]. Then, using a cavity that is far from the confocal degeneracy point, an additional quadratic phase correction is added onto the DMD transfer function to effectively bring the DMD plane to the Fourier plane of the cavity centre. Finally, any intracavity field we desire can be generated by programming its Fourier transform to be displayed on the DMD. In our experiment, we perform Bragg spectroscopy at six different momenta; the measured DMD probe fields associated with these momenta are shown in Extended Data Fig. 1. The maximum $k_\perp$ modulation we can inject is limited by the numerical aperture of the lens that in-couples the DMD light and by the piece holding the mirror.

Bragg spectroscopy and self-correlation analysis

The dynamic susceptibility of the system can be measured by using the longitudinal probe imprinted with a phase modulation $\propto k_\perp$ along $\hat{x}$ to stimulate, along with the pump fields, the scattering of atoms into the momentum states $|\Psi(k_\perp)\rangle_+ = \sum_{\sigma,\tau=\pm1} |\tau k_r + \sigma k_\perp, \sigma k_r\rangle$, as illustrated in Fig. 3a. There is another possible set of states that we do not choose to stimulate or imprint given by $|\Psi(k_\perp)\rangle_- = \sum_{\sigma,\tau=\pm1} |\tau k_r - \sigma k_\perp, \sigma k_r\rangle$; note that $|\Psi(-k_\perp)\rangle_+ = |\Psi(k_\perp)\rangle_-$. We choose $|\Psi\rangle_+$ versus $|\Psi\rangle_-$ by setting the phase of the field imprinted by the DMD. The $|\Psi\rangle_+$ state yields the phase

advancing images in the main text. Because the scattering is coherent, the total atomic state is in a superposition of $|\Psi(k_\perp)\rangle_+$ and $|0, 0\rangle$. In real space, adding the $|\Psi\rangle_+$ excitation on top of a uniform chequerboard lattice corresponds to adding a shearing lattice distortion.

We perform Bragg spectroscopy of the system's excitations by monitoring the increase in the population of the scattered atoms in the time-of-flight images versus the relative detuning between the longitudinal probe and the transverse pump. This detuning is adjusted with an acousto-optic modulator on the longitudinal probe beam path. The pump power is first ramped up to prepare the system with a given cavity-mediated interaction strength, and then the longitudinal probe beam is pulsed on for 0.5 ms. For measurements of mode-softening below the transition threshold, the response can be read out by directly counting the atom population excited into the $|\Psi\rangle_+$ momentum state. There are no background atoms at these momenta because there is no population of this momentum state in the normal phase: any atom signal is due to the Bragg excitation. The resonance frequency is extracted by fitting the spectrum to a symmetric double-Lorentzian peak. The set of such frequencies is plotted in Fig. 3e along with curves produced using the theory presented below. The blue uncertainty bands are primarily due to the atom number uncertainty in the cavity-mediated interaction strength. The bands broaden close to threshold where the photon contribution plays an increased role.

For measurements above the threshold, however, the situation is complicated by the macroscopic population of atoms already in the $|\Psi\rangle_0 = \sum_{\sigma,\tau=\pm1} |\tau k_r, \sigma k_r\rangle$ excited momentum state. While the longitudinal probe creates an additional momentum excitation, the additional atoms are hard to distinguish from that already present because (1) the number of these atoms is small compared to the number already condensed into this state; and (2) $k_\perp \ll k_r$, so that $|\Psi\rangle_+$ cannot be distinguished from $|\Psi\rangle_0$ given the limited 20-ms time-of-expansion of the time-of-flight image. Thus, the same momentum-space atom-counting method used for below-threshold spectroscopy measurements is not viable.

We therefore turn to an alternative method that uses these same absorption time-of-flight (TOF) images, but performs an analysis based on momentum correlations rather than momentum-space atom counting. To explain how this works, we first note that in real space, the longitudinal probe creates a small periodic distortion in the originally perfect chequerboard lattice. We can quantify this distortion by computing the momentum-space self-correlation $\langle \rho(\mathbf{k}+\delta\mathbf{k})\rho(\mathbf{k})\rangle$ of the atomic momentum distribution $\rho(\mathbf{k})$, which can be computed from $\langle \rho(\mathbf{r}+\delta\mathbf{r})\rho(\mathbf{r})\rangle_{\mathrm{TOF}}$ in each time-of-flight image. By focusing on the correlation between the shape of the wavepackets centred at momentum states $|\Psi\rangle_0$ and $|0, 0\rangle$, we can discern the presence of atoms excited to $\pm k_\perp$ states. This is because the correlation in the shape of $\rho(\mathbf{k})$ at $\mathbf{k} = (0, 0)$ and at the four $(\pm k_r, \pm k_r)$ regions is strongest when a perfect chequerboard lattice is present: the wavepacket of the excited momentum state $|\Psi\rangle_0$ is simply a momentum displacement of that at $\mathbf{k} = (0, 0)$. However, in the presence of a small lattice distortion given by $k_\perp$, the structure factor is reduced and destructive matter–wave interference results in a reduction in the correlation. This correlation reduction is what is plotted in the inset of Fig. 4c. The phonon mode resonances are manifest in the correlation signal dips.

To perform the above-threshold measurement, we first fit the entire image to a broad two-dimensional Gaussian profile as an estimate of the background contribution arising from atom heating and from atom scattering halos resulting from the pumps. Then the self-correlation analysis is performed on the background-subtracted images. Due to imperfect subtraction, negative values appear in parts of the correlation. Note that since we are only interested in the correlations between Bragg peaks—all positive valued—the negative values do not affect the results. This analysis is repeated for each value of probe detuning ω and $k_\perp$ to form the experimental $\omega(k_\perp)$ dispersion curve shown in Fig. 4c. Due to the sensitivity to atom number fluctuations in the correlation versus ω spectroscopy data, we perform bootstrap sampling to obtain a more reliable error estimate for the data points comprising $\omega(k_\perp)$.

Measuring spontaneous symmetry breaking of $U(1)$ symmetry

We now discuss how we measured the shot-to-shot phase fluctuations presented in Fig. 2f in the main text. In principle, the breaking of $U(1)$ symmetry can be directly measured from the phase difference between the LO beam and the cavity emission. This phase difference can be extracted from the image in a spatial heterodyne measurement, which would manifest as an overall shot-to-shot phase shift in the interference fringes in the entire image. However, the shot-to-shot relative phase between the LO and the cavity emission suffers from technical drift due to fluctuations in optical path lengths. Nevertheless, in our previous work of ref. [30], we showed that in a confocal cavity, the spatial phase difference $\Delta\phi$ between the local and non-local part of the cavity field is directly related to the phase of the atomic DW along the cavity axis ϕ_A via the relation $\phi_A = -2\Delta\phi$. With this approach of measuring relative spatial phase in cavity emission, the technical phase drift is reduced to an overall phase shift on both the local part and non-local part of the field that drops out of their difference. Computing the quantity $\Delta\phi$ in the spatial heterodyne image then cancels this overall phase drift, and the atomic DW phase ϕ_A can be measured from shot-to-shot.

As discussed in the Supplementary Information regarding time dynamics, when the power of two pump beams is balanced, the phase of the atomic density wave is allowed to freely slide along the cavity axis, which results in a substantial reduction in the spatial heterodyne signal strength for integration time longer than around 2 ms. As such, to achieve a reasonable level of signal-to-noise ratio for measuring the phase of the cavity field for both the local and non-local components, we rapidly ramp up the pump power to $\eta^2/\eta_{\mathrm{th}}^2 = 10$ in 750 μs, faster than the typical timescale of the phonon dynamics. Additionally, we employ a ~35-μm-long gas to obtain higher atomic density for further enhancing the cavity emission field amplitude. As shown in Fig. 2c in the main text, the phase of the local part of the field is taken from the peak amplitude of the electric field localized around the atoms, while the phase of the non-local part is computed from an average of a patch of the electric field off to the side of the atoms.

Data availability

The datasets generated during the current study are available in the Harvard Dataverse Repository, https://doi.org/10.7910/DVN/LGT5O6.

44. Kroeze, R. M., Guo, Y., Vaidya, V. D., Keeling, J. & Lev, B. L. Spinor self-ordering of a quantum gas in a cavity. *Phys. Rev. Lett.* **121**, 163601 (2018).

Acknowledgements We thank S. Kivelson, S. Hartnoll and V. Khemani for stimulating discussions. We acknowledge funding support from the Army Research Office. Y.G. and B.M. acknowledge funding from the Stanford Q-FARM Graduate Student Fellowship and the NSF Graduate Research Fellowship, respectively. S.G. acknowledges support from NSF grant no. DMR-1653271.

Author contributions All authors contributed to the work and contributed to writing the paper.

Competing interests The authors declare no competing interests.

Additional information

Supplementary information The online version contains supplementary material available at https://doi.org/10.1038/s41586-021-03945-x.

Correspondence and requests for materials should be addressed to Benjamin L. Lev.

Peer review information *Nature* thanks Francesco Piazza and the other, anonymous, reviewer(s) for their contribution to the peer review of this work.

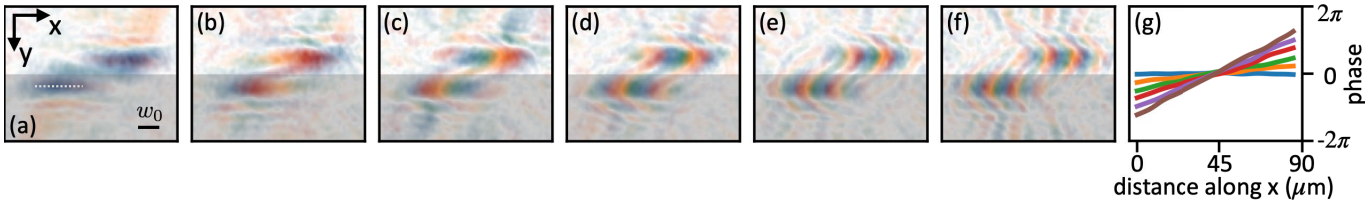

Extended Data Fig. 1 | DMD momentum probes. a–**g**, Measured DMD probe transmission cavity field and their phase profile line cuts. The values of $k_\perp/k_r$ in panels **a**–**f** are [0, 2.1, 4.2, 6.3, 8.5, 10.6] × 10^{-3}, respectively. The white dashed line in panel **a** shows the length of the cuts in panel **g**. Additional features around the main probe field are due to imperfections of the confocal cavity and stray light from the DMD probe beam. The grey area is the half plane that contains the mirror image of the probe field, and we do not show this redundant portion of the image in the main text figures.